Journal of Biomechanics 45 (2012) 2264–2270

Contents lists available at SciVerse ScienceDirect

Journal of Biomechanics

journal homepage: www.elsevier.com/locate/jbiomech
www.JBiomech.com

Spatial distribution of tissue level properties in a human femoral cortical bone

Daniel Rohrbach [a], Sannachi Lakshmanan [a], Françoise Peyrin [b], Max Langer [b], Alf Gerisch [c], Quentin Grimal [d,e], Pascal Laugier [d,e], Kay Raum [a,f,*]

[a] Julius Wolff Institute & Berlin Brandenburg School for Regenerative Therapies, Charité-Universitätsmedizin Berlin, Berlin, Germany
[b] CREATIS; CNRS UMR 5220; INSERM U1044; Université de Lyon; INSA Lyon, 69621 Villeurbanne Cedex, France
[c] Technische Universität Darmstadt, Fachbereich Mathematik, AG Numerik und wissenschaftliches Rechnen, Dolivostr. 15, 64293 Darmstadt, Germany
[d] UPMC Univ. Paris 06, UMR 7623, LIP, F-75005 Paris, France
[e] CNRS, Laboratoire d'Imagerie Paramétrique, UMR 7623, F-75006 Paris, France
[f] Dept. of Orthopedics, Martin Luther University of Halle-Wittenberg, 06097 Halle, Germany

ARTICLE INFO

Article history:
Accepted 7 June 2012

Keywords:
Acoustic microscopy
Acoustic impedance
Anisotropy
Cortical bone
Cortical porosity
Elastic properties
Microscale
Synchrotron radiation
μCT

ABSTRACT

The mechanical properties of cortical bone are determined by a combination bone tissue composition, and structure at several hierarchical length scales. In this study the spatial distribution of tissue level properties within a human femoral shaft has been investigated. Cylindrically shaped samples (diameter: 4.4 mm, $N=56$) were prepared from cortical regions along the entire length (20–85% of the total femur length), and around the periphery (anterior, medial, posterior and lateral quadrants). The samples were analyzed using scanning acoustic microscopy (SAM) at 50 MHz and synchrotron radiation micro computed tomography (SRμCT). For all samples the average cortical porosity (*Ct.Po*), tissue elastic coefficients (c_{ij}) and the average tissue degree of mineralization (*DMB*) were determined. The smallest coefficient of variation was observed for *DMB* (1.8%), followed by *BV/TV* (5.4%), c_{ij} (8.2–45.5%), and *Ct.Po* (47.5%). Different variations with respect to the anatomical position were found for *DMB*, *Ct.Po* and c_{ij}. These data address the anatomical variations in anisotropic elastic properties and link them to tissue mineralization and porosity, which are important input parameters for numerical multi-scale bone models.

© 2012 Elsevier Ltd. All rights reserved.

1. Introduction

One of the striking features of bone tissue is its ability to adapt to variable loading conditions, by tuning tissue composition and architecture of a basic building unit, the mineralized collagen fibril, at several levels of hierarchical organization through tissue remodelling, i.e., interlinked processes of permanent tissue resorption and tissue deposition. This results in spatially, temporally and directionally variable elastic properties, which in turn lead to a perfect adaptation of the tissue to locally varying functional demands. Although there is clear evidence that the cortical tissue properties in the peripheral skeleton are variable (Saied et al., 2008) due to this adaptation at the tissue scale, the problems of assessing these variations and their potential use in macroscale numerical models are still unsolved.

Elastic properties of bone are widely used in conjunction with numerical simulations, e.g., deformation (Austman et al., 2008), failure analysis (Boccaccio et al., 2008; Tomaszewski et al., 2010; Verhulp et al., 2008), fracture healing (Vetter et al., 2011), and ultrasound wave propagation (Bossy et al., 2004). Today, the most common input data come from clinical computed tomography (CT) or μCT measurements, as they are easily assessable and provide detailed 3D structural information non-destructively. However, elastic material properties cannot be derived directly from CT data. Instead, either homogenous isotropic material properties or empirical Hounsfield-to-Young's modulus conversion rules have been applied to assign elastic properties to the mineralized tissue matrix(Austman et al., 2008). Today, it is well accepted that the scalar Hounsfield quantity represents a combination of local tissue mineralization and porosity, and is therefore not able to predict directional dependencies of elastic properties, which are described by the elastic stiffness tensor. For example, Austman et al. (2009) have compared several popular conversion rules and found 50% variation for a typical Hounsfield value of cortical bone depending on the used model. They conclude that customized density-modulus relationships for specific bones may improve the accuracy of finite element models.

* Corresponding author at: Julius Wolff Institute & Berlin Brandenburg School for Regenerative Therapies, Charité-Universitätsmedizin Berlin, Augustenburger Platz 1, D-13353 Berlin, Germany. Tel.: +49 30 450 539503; fax: +49 30 450 539952.
E-mail address: kay.raum@charite.de (K. Raum).

0021-9290/$ - see front matter © 2012 Elsevier Ltd. All rights reserved.
http://dx.doi.org/10.1016/j.jbiomech.2012.06.003

Due to the lack of real heterogeneous and anisotropic material properties, simplified (i.e., isotropic and homogenous) material models have often been used to study stress and strain distributions under physiological loading conditions by finite element analyses (Duda et al., 1998; Sverdlova and Witzel, 2010). These investigations revealed inhomogeneous stress patterns within the femoral shaft. Experimentally, anatomical variations of macroscopic elastic properties (i.e., at a length scale of a few mm) have been observed across multiple donors by 2.25 MHz contact ultrasound (Rudy et al., 2011). Bensamoun et al. (2004a, 2004b) have used a pulse-transmission technique with 5 MHz focused immersion transducers, which allowed the scanning of multiple cross-sections obtained from a single human donor. By combining the acoustic compressional wave velocity maps with porosity data obtained by scanning electron microscopy, they observed a significant increase of the velocity with decreasing porosity. However, the acoustic wavelength in the frequency range between 1 and 5 MHz is much larger than the typical diameter of the Haversian canals. Therefore, the properties measured in this frequency range represent the compound properties of the tissue matrix and the porous network, but the individual contributions of porosity and matrix elasticity cannot be decoupled.

Tissue level properties have been assessed by site-matched measurements of the degree of mineralization of bone (*DMB*) and the acoustic impedance (*Z*) by synchrotron radiation μCT (SRμCT) and by 50–200 MHz scanning acoustic microscopy (SAM), respectively (Raum et al., 2006, 2007). The spatial resolution of both techniques is sufficient to resolve the Haversian canals (Granke et al., 2011) and provide complementary information of tissue mineralization, the anisotropic elastic tissue properties and the porous structure. With this information, the effective (mesoscale) elastic properties of the tissue compound can be derived by numerical or analytical homogenization approaches (Dong and Guo, 2006; Grimal et al., 2008, 2011b, 2011a; Hellmich et al., 2004; Parnell and Grimal, 2009). Recently, Granke et al. (2011) have combined low-frequency contact ultrasound measurements with 50 MHz SAM and SRμCT measurements of cortical femoral samples from elderly women and found that the change in the intra-cortical porosity accounts for most of the variations of the compound elastic properties. This assumption has further been supported by a cross-sectional study by Zebaze et al. (2010), who have suggested cortical porosity to be a major determinant of non-vertebral fracture risk.

Novel emerging in-vivo technologies, e.g., quantitative ultrasound (QUS) (Laugier, 2008; Raum et al., 2005) and ultra-short echo-time magnetic resonance imaging (MRI) (Rad et al., 2011) are sensitive to both structural and elastic variations. However, an independent assessment of cortical porosity would be of key diagnostic interest. For the future development and validation of these technologies, reliable decoupled data of cortical porosity and matrix properties are required.

In this study, a systematic investigation of a human femoral shaft has been conducted by 50 MHz SAM and site-matched SRμCT. The aim of this study was to investigate anatomical variations of Haversian porosity, tissue mineralization and elastic properties. We hypothesized that (i) there exists no global relation between tissue porosity, mineralization and elastic properties, (ii) the dependencies of tissue composition, structural and elastic properties on the anatomical location may not be similar, and (iii) an elastic adaptation to macroscopic mechanical conditions occurs at the tissue level.

1.1. Theoretical background of parameter extraction

The principles of the acoustic data acquisition and the conversion of the measured reflection amplitude to acoustic impedance and elastic coefficients have been described elsewhere (Lakshmanan et al., 2007; Raum et al., 2003, 2004; Raum, 2008) and are summarized in the appendix.

2. Materials and methods

2.1. Sample preparation

The shaft of one human femur (female, 72 years) was divided into 14 cross sections from proximal to distal (Fig. 1). The thickness of each section was 22 mm. All sections were dehydrated in a graded series of ethanol (70%, 96% and 100%, immersion for 24 h in each solution) and embedded in PMMA. The cross-sectional surfaces of the discs were ground with successively decreasing grain size (SiC paper 2400 and 4000; Struers GmbH, Willich, Germany) and a final polishing step (Logitech WG2, Struers GmbH, Willich, Germany) with a hard synthetic cloth (Microtex 500, Struers GmbH, Willich, Germany), ethyleneglycol suspension and 3 μm diamond particles as abrasive. After the cross-sectional scan the discs were further divided into posterior, medial, anterior and lateral sections. For each quadrant, one transverse surface was prepared and scanned, as described above. Finally, from each quadrant ($N=56$), one cylindrically shaped sample with a diameter of 4.4 mm, where the orientation of the long axis was parallel to the radial axis of the femur shaft (Fig. 1). The samples were drilled using a high precision lathe equipped with a diamond milling knife. The final surface smoothness of the cylinder surfaces was obtained by grinding with successively decreasing grain size (SiC paper 2400 and 4000).

Ethical approval for collection of samples was granted by the Ethics Committee of the Medical Faculty of Martin Luther University (Halle, Germany). The legal guardian of the tissue donor provided informed written consent to provide their tissues for investigation.

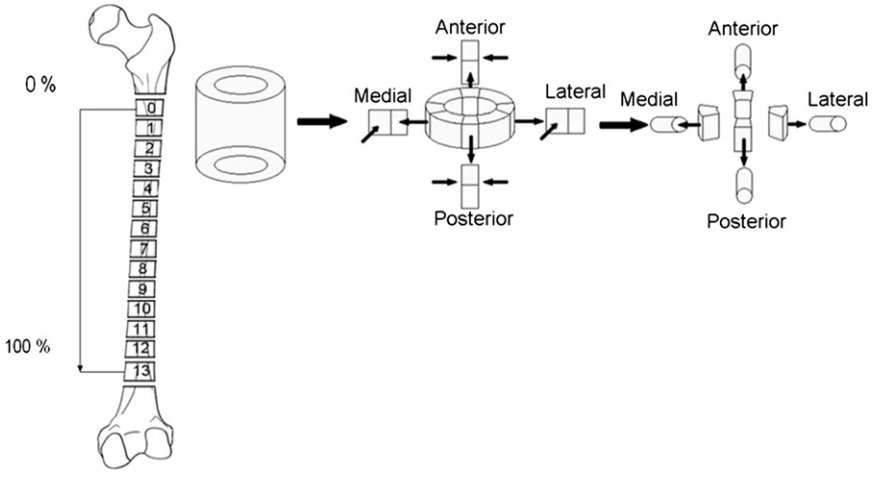

Fig. 1. Schematic illustration of the sample preparation.

2.2. Scanning acoustic microscopy

Our custom scanning acoustic microscope (SAM200Ex, Q-BAM, Halle, Germany) was equipped with a spherically focussed 50 MHz transducer (V605/60°, Valpey Fisher, Hopkinton, MA) that provides a lateral resolution of 23 μm in the focal plane. Calibrated scans of the confocal reflection amplitude of the flat and cylindrically shaped samples were performed, as described in Lakshmanan et al. (2007), Raum (2008). For the cylinder scans, a rotational stage (DT-80; Micos GmbH, Eschbach, Germany) and a custom made sample holder were attached to the microscope. An eccentricity compensation during the scan of cylinder samples was implemented in the acquisition software (Lakshmanan et al., 2007). All measurements were performed in a temperature controlled water tank. As coupling fluid distilled and degassed water at 25 °C was used.

The radio frequency ultrasound signals were digitized at a sampling rate of 500 MHz. The recorded surface reflection amplitudes were converted into values of acoustic impedance using a time-of-flight (TOF) based defocus correction and impedance calibration procedure, as described elsewhere (Raum, 2008). Examples of calibrated impedance maps are shown in Fig. 2.

2.3. Synchrotron radiation μCT

After SAM inspection, the samples were imaged using SRμCT on beamline ID19 at the ESRF (European Synchrotron Radiation Facility, Grenoble, France). We selected an isotropic voxel size of 10.1 μm and a field of view of 6.06×6.06 mm^2. The energy was set to 26 keV with a bandwidth $\Delta E/E$ of 10^{-4} by using a double Si-crystal monochromator set to reflect in the vertical plane. For each sample, radiographic images over 1600 angles of view were recorded. The details of the tomographic reconstruction and conversion to *DMB* and mass density are provided in the online supplement.

All post processing of the SAM data and the reconstructed SRμCT volumes was done using custom toolboxes developed with Matlab R2007a (The Mathworks Inc., Natick, MA, USA).

2.4. Image segmentation and parameter extraction

Several steps were necessary to ensure a site-matched analysis of the SAM and SRμCT images. In each 3D reconstructed SRμCT volume, the outer cylinder surfaces were detected and the data were transformed by translation and rotation operations in order to align the long axis of the cylinders with the x_1 (cylinder) axis of a cylindrical coordinate system (Fig. 3). In the acoustic images, the mineralized tissue was segmented from the outer tissue boundaries and Haversian canals using adaptive threshold masks, as described by Lakshmanan et al. (2007). Thresholds were set to the local mean impedance value of osteonal tissue and PMMA. For the synchrotron data, we have developed a 3D segmentation and erosion algorithm to minimize the influence of the partial volume effect. The unwrapped $Z(x_1,\theta)$ images of the cylinder surfaces were registered with the surface *DMB* maps extracted from the SRμCT volume data (Fig. 3) using the image registration tools of Matlab R2007a (The Mathworks Inc., Natick, MA, USA).

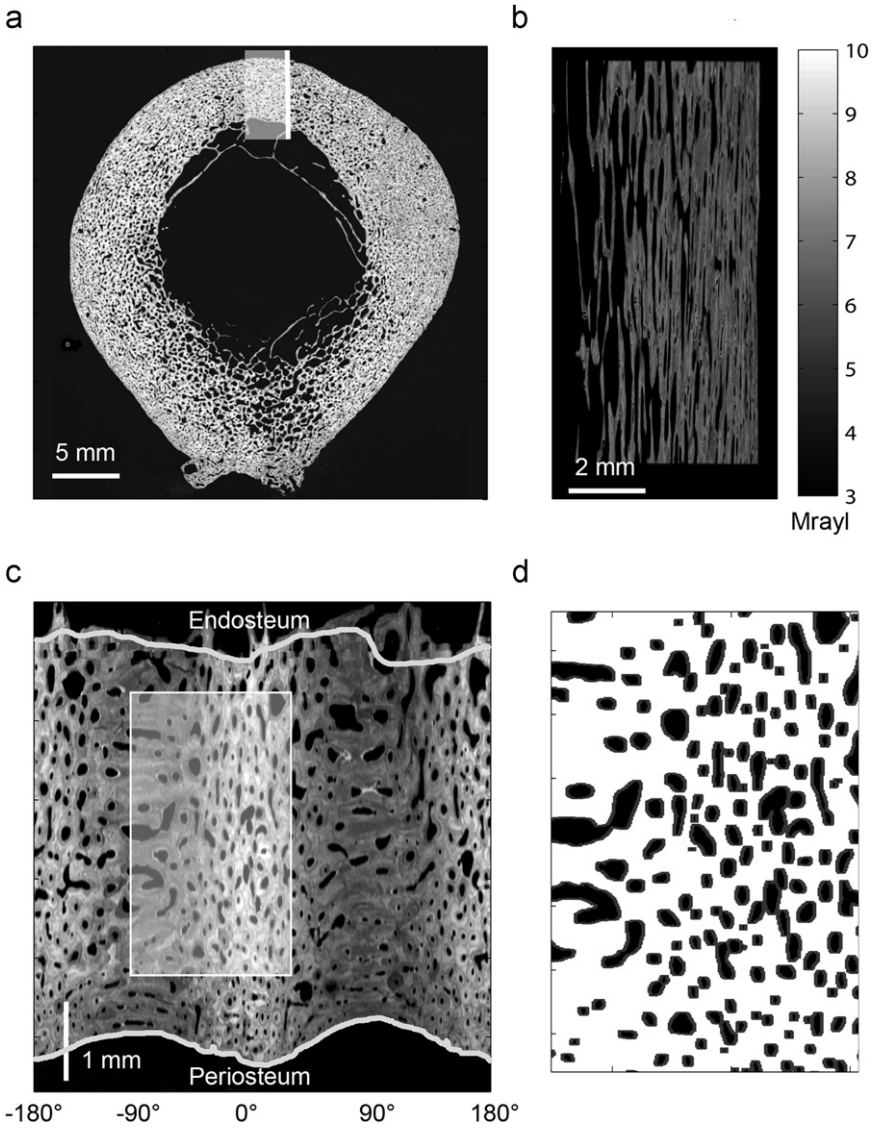

Fig. 2. Acoustic impedance images of a cross-section (a), transverse section (b) and a cylinder sample (c). The line and the highlighted rectangle in (a) indicate the region for the transverse sectional scan and the cylinder measurement, respectively. For better illustration the cylinder surface was unwrapped. A segmented and eroded image is shown in (d) for the small region highlighted in (c). While the periosteal boundary (lower line) was detected automatically by the threshold procedure, the endosteal boundary (upper line) has been drawn manually to ensure proper exclusion of trabecular tissue.

This image preprocessing allowed direct comparison of averaged *DMB* and $Z(\theta)$ within identical volumes of interest (VOI). Within these volumes, cortical porosity *Ct.Po*, *DMB* and c_{ij} were extracted.

Ct.Po (%) was defined as the ratio between the volume filled by the Haversian canals and the total selected bone volume. Similarly, the bone volume fraction *BV/TV* (%) is 100%-*Ct.Po* (%). The mean tissue *DMB* was determined from the segmented and eroded mineralized tissue voxels within the VOI. Note that *Ct.Po*, *BV/TV* and *DMB* were determined from the entire cortical tissue within the 3D volume data.

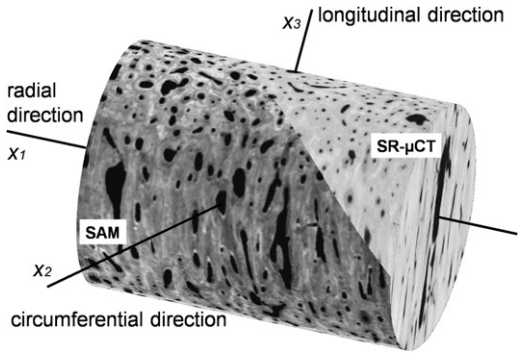

Fig. 3. Example of site-matched SAM and synchrotron μCT data. The grey levels correspond to *DMB* in the volumetric SRμCT data and to $Z(\theta)$ in the SAM data. Both methods allow a reliable segmentation of the Haversian canal network. Moreover, a directional dependence is evident for $Z(\theta)$, but not for *DMB*.

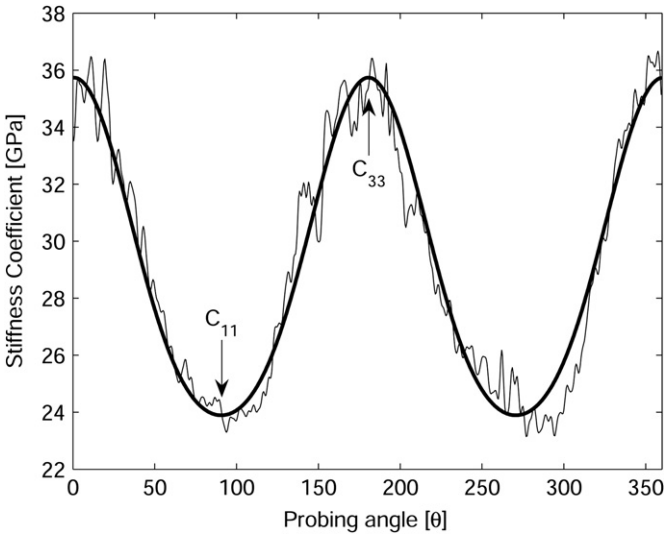

Fig. 4. Example of a fit of the measured data to a transverse isotropic model. The correlation coefficient was $R^2=0.98$.

The unwrapped $Z(x_1,\theta)$ maps exhibit a characteristic variation of Z with respect to the observation angle θ (Fig. 2c and Fig. 3). Each pixel represents a single elastic measurement at the surface of the sample. Surface diameter and thickness contributing to the elastic interaction with the acoustic pulse are equivalent to the beam diameter (i.e., 23 μm) and the wavelength (i.e., approximately 70 μm). For each angle θ, the segmented impedance values were averaged over x_1 and converted to $c(\theta)$ using Eq. (A4). The fit of the measured $c(\theta)$ to a transverse isotropic model (Eq. (A2)) yields the axial elastic coefficients c_{33}, the radial elastic coefficient c_{11}, and $c^*=c_{13}+2c_{44}$ (Fig. 4). The coefficients c_{12} and c_{13} were extracted using continuum micro-mechanical model constraints as described by Lakshmanan et al. (2007). The remaining elastic coefficient c_{44} was calculated from c^*. Note that the elastic coefficients were estimated from the cylinder surface measurements and not from the cylinder volume.

2.5. Statistical analysis

Data are presented as mean ± standard deviation. Linear, nonlinear and multivariate regression analyses and ANOVA followed by post-hoc multi-comparison Tukey tests were used to evaluate anatomical influences on the derived tissue properties. All statistical results were considered significant for *p*-values less than 0.05. The statistical computations were made using the Matlab Statistics Toolbox (The Mathworks Inc., Natick, MA, USA).

3. Results

The spatial fusion of SR-μCT and SAM data of one sample is shown in Fig. 3. It can be seen that at the chosen spatial resolution both methods resolve the Haversian canal network, but not the osteocyte lacunae. Differences between osteonal and interstitial tissues are visible both in *DMB* and *Z* maps. As expected, a characteristic dependence on the orientation θ is evident in the surface maps of $Z(x_1,\theta)$, but not in those of $DMB(x_1,\theta)$ (data not shown).

The average values and ranges of *DMB*, elastic coefficients and technical constants of all samples are listed in Table 1. The anisotropy ratio $ar=c_{33}/c_{11}$ was predominantly determined by a variation of c_{33} ($R^2=0.25$), but not by that of c_{11} ($R^2=0.09$). Moreover, we observed a minor increase of *ar* with increasing degree of mineralization ($R^2=0.29$). The three experimentally derived elastic parameters were highly correlated ($0.37 \le R^2 \le 0.55$). Therefore, a reasonable approximation of the elastic tensor (except for c_{44}) was possible based on the stiffness values measured in only one direction, e.g., from transverse (c_{11}) or from cross (c_{33}) sections (Table 2).

Tissue mineralization, density and *ar* were lower in the posterior region than in the medial and lateral regions. By contrast, the highest

Table 1
Summary of tissue level properties. For comparison with literature data, also the technical constants E1 and E3 and the Poisson ratios γ_{ij} were derived from the elastic coefficients c_{ij}. For significant variations between the circumferential regions the ANOVA *F*-statistic, *p*-value, and the result of the Tukey test are provided. The last column indicates directional changes in the axial direction, as revealed by linear or nonlinear regression analysis.

		Circumferential position	Tukey test	Axial position
DMB [g/cm^3]	1.11 ± 0.02	$F=3.64$, $p=0.018$	$P<M,L$	Central > Prox, Dist., $R^2=0.83$
ρ [g/cm^3]	1.93 ± 0.01	$F=3.64$, $p=0.018$	$P<M,L$	Central > Prox, Dist., $R^2=0.83$
Ct.Po [%]	10.1 ± 4.8	$F=5.98$, $p=0.001$	$P>A,L$	Prox > Dist, $R^2=0.71$
Z_3 [Mrayl]	7.97 ± 0.37	n.s.	n.a.	Prox < Dist, $R^2=0.48$
Z_1 [Mrayl]	6.75 ± 0.28	n.s.	n.a.	Prox < Dist, $R^2=0.39$
c_{33} [GPa]	33.0 ± 3.0	n.s.	n.a.	Prox < Dist, $R^2=0.43$
c_{11} [GPa]	23.7 ± 1.94	n.s.	n.a.	Prox < Dist, $R^2=0.38$
c_{12} [GPa]	9.5 ± 1.2	n.s.	n.a.	Prox < Dist, $R^2=0.48$
c_{13} [GPa]	10.0 ± 1.3	n.s.	n.a.	Prox < Dist, $R^2=0.48$
$c_{44}=G_{13}$ [GPa]	6.6 ± 3.0	n.s.	n.a.	Prox < Dist, $R^2=0.36$
E_3 [GPa]	26.1 ± 2.5	n.s.	n.a.	Prox < Dist, $R^2=0.50$
E_1 [GPa]	18.5 ± 1.8	n.s.	n.a.	Prox < Dist, $R^2=0.34$
γ_{12}	0.31 ± 0.02	$F=6.12$, $p=0.001$	$P<A,M,L$	n.s.
γ_{13}	0.22 ± 0.01	$F=6.97$, $p=0.00051$	$P>A,M,L$	n.s.
γ_{31}	0.32 ± 0.01	$F=3.97$, $p=0.001$	$P<M$	n.s.
$ar=c_{33}/c_{11}$	1.4 ± 0.1	$F=7.38$, $p=0.0003$	$P<A,M,L$	Central > Prox, Dist., $R^2=0.51$

Ct.Po was found in the posterior region. Other significant variations between the circumferential regions are summarized in Table 1. Variations of tissue mineralization, porosity and elastic properties were also found be different along the axial direction. *DMB* and ρ increased from the proximal region towards the mid-diaphysis, and only marginally decreased towards the distal end (Fig. 5a). A reverse trend was observed for *Ct.Po* (Fig. 5b). However, all elastic coefficients increased from the proximal to the distal regions (Fig. 5c). The highest anisotropy ratio *ar* was found in the mid-diaphyseal region of the femoral shaft and decreased towards the proximal and distal sides (Fig. 5d). The regression coefficients for all parameters are summarized in Table 1.

4. Discussion

This study presents the first systematic survey of microstructure, tissue mineralization, and anisotropic elastic properties of the cortical tissue matrix within a human femoral shaft. Tissue embedding is a standard procedure for micro-elastic investigations of bone tissue (Manjubala et al., 2009; Raum, 2008) and has been chosen in the current investigation as it provides long-term tissue fixation as well as easy sample preparation using standard metallographic techniques. These conditions were required (i) to ensure sample durability between the acoustic and x-ray investigations and (ii) to produce smooth surfaces of the cylindrical surfaces for the acoustic evaluation.

Table 2
Prediction of the tissue level elastic tensor based on elastic parameters measured in the cross (c_{33}) and transverse (c_{11}) sections.

c_{33} [GPa]	R^2	RMSE [GPa]	c_{11} [GPa]	R^2	RMSE [GPa]
$c_{11}=0.43\ c_{33}+9.36$	0.44	1.46	$c_{33}=1.02\ c_{11}+8.73$	0.44	2.24
$c_{12}=0.22\ c_{33}+2.58$	0.99	0.03	$c_{12}=0.22\ c_{11}+4.62$	0.43	0.50
$c_{13}=0.22\ c_{33}+3.44$	0.99	0.03	$c_{13}=0.22\ c_{11}+5.49$	0.43	0.51
$c_{44}=0.18\ c_{33}+1.25$	0.18	1.14	$c_{44}=0.43\ c_{11}-3.00$	0.45	0.94

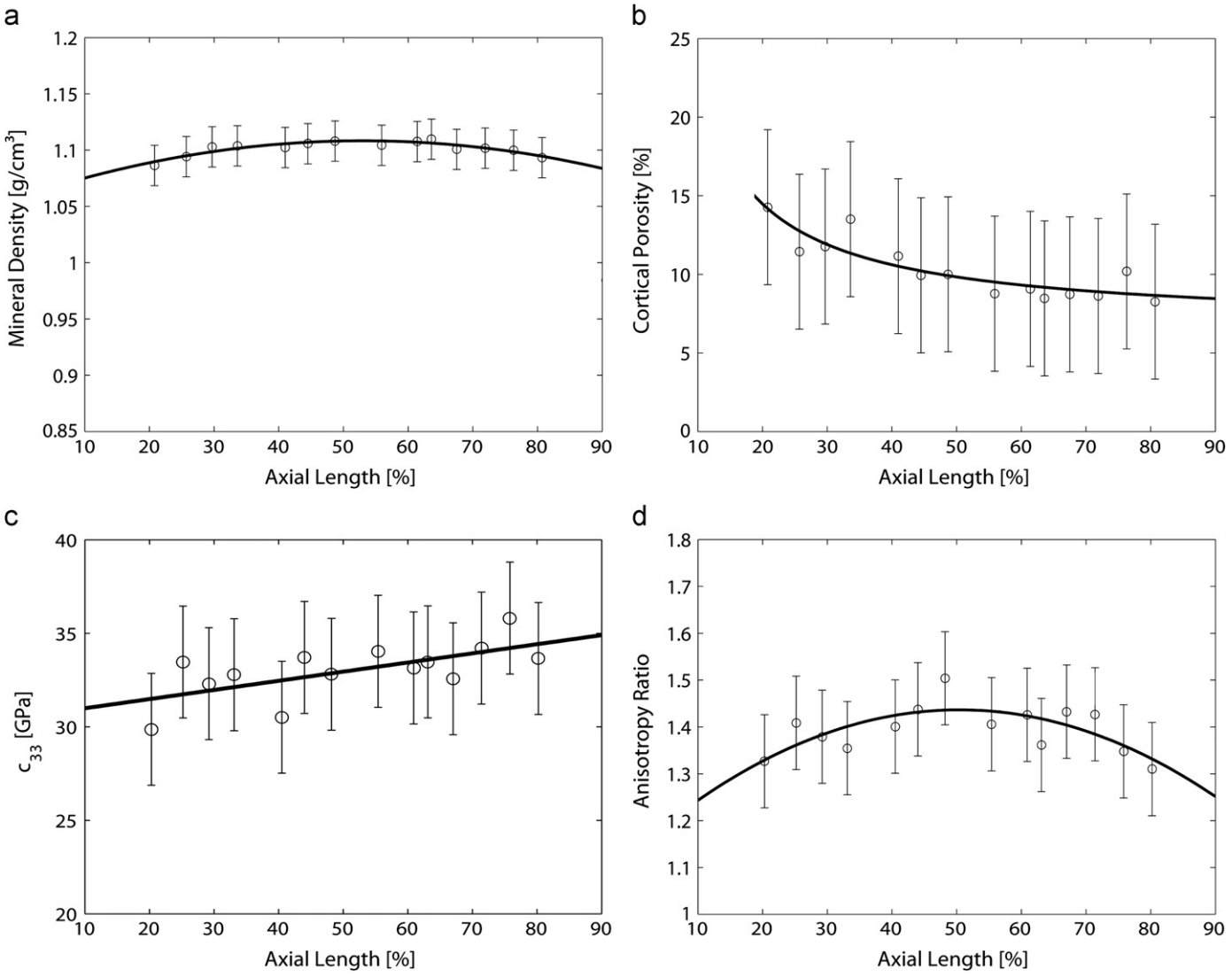

Fig. 5. Variations of selected tissue level properties along the axial position.

The replacement of water by the embedding material may increase both mass density and the elastic properties of the tissue. The relationship between *DMB* and mass density has been evaluated by Raum et al. (2007) and has been incorporated in this study. Zimmerman et al. (1994) have analysed the effect of embedding on the acoustic impedance in bovine tissue. They found a consistent increase in the acoustic impedance in the order of 4%, or around 8% after conversion to apparent stiffness values via Eq. (A4). It should be noted that the relative increase of material properties depends on the amount of water that can be replaced by the embedding material. For example, tissue with a high degree of mineralization contains less water than tissue with a low degree of mineralization. The samples investigated in this study exhibited a very low variation of *DMB* (coefficient of variation $CV=1.8\%$). Therefore, the reported mass densities and elastic properties presented are presumably biased, but the relative variations with respect to the anatomical locations can be considered not to be influenced by the embedding process. Indeed, the estimated absolute values and anatomical variations of material properties and tissue porosity are consistent with previously reported data. For example, Rho et al. (1999) have measured the Young's modulus E_3 by nanoindentation in embedded samples of human femoral cortical bone tissue of donors of various ages. The diameter of the surface interaction area with the indenter of approximately 5 μm was comparable to the SAM-resolution in our study. They reported values in the range from 18 GPa in osteonal tissue to 27 GPa in interstitial tissue. Ashman et al. (1984) observed that density was greater in the central part than in the proximal region. Similar to all previous investigations, the proximal posterior region exhibits the lowest density, highest porosity and the lowest stiffness values (Ashman et al., 1984; Bensamoun et al., 2004b; Espinoza Orias et al., 2009; Weiss et al., 1998). Other variations, e.g., the dependence of the anisotropy ratio *ar* on the long axis position were different compared to those measured by low-frequency ultrasound (Rudy et al., 2011). A potential explanation for the different relationships of tissue level and macroscopic anisotropy ratios may be the different anatomical variations of tissue mineralization, elastic properties, and porosity observed in this study. It should also be noted that in this study the major orientation of the Haversian canals was always defined as the x_3-direction. Particularly in the proximal and distal epiphyses, the orientations of the Haversian canals are considerably tilted relative to the long axis of the femur. For a direct comparison, homogenization models that take into account the matrix properties, porosity, and pore structure are necessary (Grimal et al., 2011b).

Interestingly, tissue mineralization does not always vary in a similar way as the elastic coefficients between the anatomical regions. The variation of *ar* along the axial direction can be explained by a change of the ultra-structural arrangement of the mineralized fibrils relative to the bone long axis, whereas the highest values correspond to a higher degree of fibril alignment with the bone axis. This is reasonable, since the central region requires the highest ultimate tensile strength and compressional stiffness due to tensile muscle forces and weight bearing under physiological loading conditions (Duda et al., 1998), while the proximal and distal regions are more exposed to bending and torsion.

The lowest variance was observed for *DMB*. This finding is consistent with previous investigations at the human radius (Raum et al., 2005) and the human trochanter (Zebaze et al., 2011). Bone mineral density distributions (BMDD) have been extensively investigated by quantitative backscattered electron microscopy (qBEI). Reference data exist for trabecular BMDD from iliac crest samples of adults for healthy, diseased and various treatment conditions (Roschger et al., 2008). In healthy subjects, the coefficient of variation *CV* is small (2.1% for 52 individuals). Lower distribution values have been observed in subjects suffering from osteoporosis and mild primary hyperparathyroidism, while a shift towards higher mineralization was found in subjects with osteogenesis imperfecta. A slight shift towards lower values (-5.6%) has also been observed in iliac crest biopsies of children, adolescent and young adults (Fratzl-Zelman et al., 2009). Within the femoral shaft investigated in this study, we found that variations with respect to the anatomical position were different for *DMB* and elastic coefficients. This supports the hypothesis that no global relation between tissue mineralization and tissue elastic properties exists. Instead, it appears that despite a fairly constant mineralization at the microscale, elastic adaptation in the order of 7% is achieved by variations of the matrix *ar*. Moreover, significant correlations that have been observed, even between the independently assessed parameters (c_{11}, c_{33}, c^*). Therefore the assessment of one or two coefficients, e.g., in the transverse and cross-sectional planes may be sufficient for a reasonable approximation of the transverse isotropic stiffness tensor for particular tissue types and anatomical locations. In combination with analytical (Grimal et al., 2011b; Parnell and Grimal, 2009) or numerical (Grimal et al., 2008) homogenization techniques, a rapid evaluation of the complex interplay between structural, compositional and elastic adaptation is possible. In this study, we have shown that variations of cortical porosity and microscale elastic properties of the tissue matrix are much stronger than variations of tissue mineralization. Although our investigation on one healthy elderly subject does not allow to draw a general conclusion on the role cortical porosity plays on fracture risk, it does support the findings of a cross-sectional study by Zebaze et al. (2010), who suggested that cortical porosity may be an important indicator for the identification of individuals at high risk of fracture.

5. Conclusions

The relations between anisotropic elastic coefficients, degree of mineralisation and cortical porosity at the tissue level have been investigated in a human femoral shaft. Remarkable variations of cortical porosity and elastic properties have been observed, while the degree of mineralization was fairly invariable. We postulate that the observed heterogeneity of tissue properties is linked to variable mechanical loading conditions within the femoral shaft. In addition to other factors required for reliable FE simulations, e.g., accuracy of the mesh generation and refinement, knowledge of the load and boundary conditions, the variations of microstructural and anisotropic elastic properties of the tissue matrix observed in this study are likely to have a considerable effect on the reliability of numerical models. In combination with analytical or numerical homogenization techniques, a rapid evaluation of the complex interplay between structural, compositional and elastic adaptation is possible, which may open directions for a differential diagnosis of bone properties.

Conflict of interest statement

All authors have no conflict of interest and nothing to disclose.

Acknowledgments

This work has been conducted within the European Associated Laboratory "Ultrasound Based Assessment of Bone" (ULAB) and was supported by the Deutsche Forschungsgemeinschaft (SPP 1420, grants Ra1380/7 and Ge1894/3) and the ESFR Long Term Proposal MD239.

Appendix A. Supplementary material

Supplementary data associated with this article can be found in the online version at http://dx.doi.org/10.1016/j.jbiomech.2012.06.003.

References

Ashman, R.B., Cowin, S.C., Rho, J.Y., Van Buskirk, W.C., Rice, J.C., 1984. A continous wave technique for the measurement of the elastic properties of cortical bone. Journal of Biomechanics 17, 349–361.

Austman, R.L., Milner, J.S., Holdsworth, D.W., Dunning, C.E., 2008. The effect of the density-modulus relationship selected to apply material properties in a finite element model of long bone. Journal of Biomechanics 41, 3171–3176.

Austman, R.L., Milner, J.S., Holdsworth, D.W., Dunning, C.E., 2009. Development of a customized density–modulus relationship for use in subject-specific finite element models of the ulna. In: Proceedings of the Institution of Mechanical Engineers. Part H 223, pp. 787–794.

Bensamoun, S., Gherbezza, J.M., de Belleval, J.F., Tho, M. C., Ho Ba, 2004a. Transmission scanning acoustic imaging of human cortical bone and relation with the microstructure. Clinical Biomechanics 19, 639–647.

Bensamoun, S., Tho, Ho Ba, Luu, M.C., Gherbezza, S., de Belleval, J. F., J.M., 2004b. Spatial distribution of acoustic and elastic properties of human femoral cortical bone. Journal of Biomechanics 37, 503–510.

Boccaccio, A., Vena, P., Gastaldi, D., Franzoso, G., Pietrabissa, R., Pappalettere, C., 2008. Finite element analysis of cancellous bone failure in the vertebral body of healthy and osteoporotic subjects. In: Proceedings of the Institution of Mechanical Engineers. Part H 222, pp. 1023–1036.

Bossy, E., Talmant, M., Laugier, P., 2004. Three-dimensional simulations of ultrasonic axial transmission velocity measurement on cortical bone models. Journal of the Acoustical Society of America 115, 2314–2324.

Dong, X.N., Guo, X.E., 2006. Prediction of cortical bone elastic constants by a two-level micromechanical model using a generalized self-consistent method. Journal of Biomechanical Engineering 128, 309–316.

Duda, G.N., Heller, M., Albinger, J., Schulz, O., Schneider, E., Claes, L., 1998. Influence of muscle forces on femoral strain distribution. Journal of Biomechanics 31, 841–846.

Espinoza Orias, A.A., Deuerling, J.M., Landrigan, M.D., Renaud, J.E., Roeder, R.K., 2009. Anatomic variation in the elastic anisotropy of cortical bone tissue in the human femur. Journal of the Mechanical Behavior of Biomedical Materials 2, 255–263.

Fratzl-Zelman, N., Roschger, P., Misof, B.M., Pfeffer, S., Glorieux, F.H., Klaushofer, K., Rauch, F., 2009. Normative data on mineralization density distribution in iliac bone biopsies of children, adolescents and young adults. Bone 44, 1043–1048.

Granke, M., Grimal, Q., Saied, A., Nauleau, P., Peyrin, F., Laugier, P., 2011. Change in porosity is the major determinant of the variation of cortical bone elasticity at the millimeter scale in aged women. Bone 49, 1020–1026.

Grimal, Q., Raum, K., Gerisch, A., Laugier, P., 2008. Derivation of the mesoscopic elasticity tensor of cortical bone from quantitative impedance images at the micron scale. Computer Methods in Biomechanics and Biomedical Engineering 11, 147–157.

Grimal, Q., Raum, K., Gerisch, A., Laugier, P., 2011a. A determination of the minimum sizes of representative volume elements for the prediction of cortical bone elastic properties. Biomechanics and Modeling in Mechanobiology 10, 925–937.

Grimal, Q., Rus, G., Parnell, W.J., Laugier, P., 2011b. A two-parameter model of the effective elastic tensor for cortical bone. Journal of Biomechanics 44, 1621–1625.

Hellmich, C., Ulm, F.J., Dormieux, L., 2004. Can the diverse elastic properties of trabecular and cortical bone be attributed to only a few tissue-independent phase properties and their interactions? Arguments from a multiscale approach. Biomechanics and Modeling in Mechanobiology 2, 219–238.

Lakshmanan, S., Bodi, A., Raum, K., 2007. Assessment of anisotropic tissue elasticity of cortical bone from high-resolution, angular acoustic measurements. IEEE Transactions on Ultrasonics, Ferroelectrics, and Frequency Control 54, 1560–1570.

Laugier, P., 2008. Instrumentation for in vivo ultrasonic characterization of bone strength. IEEE Transactions on Ultrasonics, Ferroelectrics, and Frequency Control 55, 1179–1196.

Manjubala, I., Liu, Y., Epari, D.R., Roschger, P., Schell, H., Fratzl, P., Duda, G.N., 2009. Spatial and temporal variations of mechanical properties and mineral content of the external callus during bone healing. Bone 45, 185–192.

Parnell, W.J., Grimal, Q., 2009. The influence of mesoscale porosity on cortical bone anisotropy. Investigations via asymptotic homogenization. Journal of the Royal Society Interface 6, 97–109.

Rad, H.S., Lam, S.C., Magland, J.F., Ong, H., Li, C., Song, H.K., Love, J., Wehrli, F.W., 2011. Quantifying cortical bone water in vivo by three-dimensional ultra-short echo-time MRI. NMR in Biomedicine 24, 855–864.

Raum, K., 2008. Microelastic imaging of bone. IEEE Transactions on Ultrasonics, Ferroelectrics, and Frequency Control 55, 1417–1431.

Raum, K., Hofmann, T., Leguerney, I., Saied, A., Peyrin, F., Vico, L., Laugier, P., 2007. Variations of microstructure, mineral density and tissue elasticity in B6/C3H mice. Bone 41, 1017–1024.

Raum, K., Jenderka, K.V., Klemenz, A., Brandt, J., 2003. Multilayer analysis: quantitative scanning acoustic microscopy for tissue characterization at a microscopic scale. IEEE Transactions on Ultrasonics, Ferroelectrics, and Frequency Control 50, 507–516.

Raum, K., Leguerney, I., Chandelier, F., Bossy, E., Talmant, M., Saied, A., Peyrin, F., Laugier, P., 2005. Bone microstructure and elastic tissue properties are reflected in QUS axial transmission measurements. Ultrasound in Medicine and Biology 31, 1225–1235.

Raum, K., Leguerney, I., Chandelier, F., Talmant, M., Saied, A., Peyrin, F., Laugier, P., 2006. Site-matched assessment of structural and tissue properties of cortical bone using scanning acoustic microscopy and synchrotron radiation μCT. Physics in Medicine and Biology 51, 733–746.

Raum, K., Reisshauer, J., Brandt, J., 2004. Frequency and resolution dependence of the anisotropic impedance estimation in cortical bone using time-resolved scanning acoustic microscopy. Journal of Biomedical Materials Research Part A 71A, 430–438.

Rho, J.Y., Zioupos, P., Currey, J.D., Pharr, G.M., 1999. Variations in the individual thick lamellar properties within osteons by nanoindentation. Bone 25, 295–300.

Roschger, P., Paschalis, E.P., Fratzl, P., Klaushofer, K., 2008. Bone mineralization density distribution in health and disease. Bone 42, 456–466.

Rudy, D.J., Deuerling, J.M., Espinoza Orias, A.A., Roeder, R.K., 2011. Anatomic variation in the elastic inhomogeneity and anisotropy of human femoral cortical bone tissue is consistent across multiple donors. Journal of Biomechanics 44, 1817–1820.

Saied, A., Raum, K., Leguerney, I., Laugier, P., 2008. Spatial distribution of anisotropic acoustic impedance assessed by time-resolved 50-MHz scanning acoustic microscopy and its relation to porosity in human cortical bone. Bone 43, 187–194.

Sverdlova, N.S., Witzel, U., 2010. Principles of determination and verification of muscle forces in the human musculoskeletal system: muscle forces to minimise bending stress. Journal of Biomechanics 43, 387–396.

Tomaszewski, P.K., Verdonschot, N., Bulstra, S.K., Verkerke, G.J., 2010. A comparative finite-element analysis of bone failure and load transfer of osseointegrated prostheses fixations. Annals of Biomedical Engineering 38, 2418–2427.

Verhulp, E., van, R.B., Muller, R., Huiskes, R., 2008. Indirect determination of trabecular bone effective tissue failure properties using micro-finite element simulations. Journal of Biomechanics 41, 1479–1485.

Vetter, A., Liu, Y., Witt, F., Manjubala, I., Sander, O., Epari, D.R., Fratzl, P., Duda, G.N., Weinkamer, R., 2011. The mechanical heterogeneity of the hard callus influences local tissue strains during bone healing: a finite element study based on sheep experiments. Journal of Biomechanics 44, 517–523.

Weiss, S., Zimmerman, M.C., Harten, R.D., Alberta, F.G., Meunier, A., 1998. The acoustic and structural properties of the human femur. Journal of Biomechanical Engineering 120, 71–76.

Zebaze, R.M., Ghasem-Zadeh, A., Bohte, A., Iuliano-Burns, S., Mirams, M., Price, R.I., Mackie, E.J., Seeman, E., 2010. Intracortical remodelling and porosity in the distal radius and post-mortem femurs of women: a cross-sectional study. Lancet 375, 1729–1736.

Zebaze, R.M., Jones, A.C., Pandy, M.G., Knackstedt, M.A., Seeman, E., 2011. Differences in the degree of bone tissue mineralization account for little of the differences in tissue elastic properties. Bone 48, 1246–1251.

Zimmerman, M.C., Prabhakar, A., Chokshi, B.V., Budhwani, N., Berndt, H., 1994. The acoustic properties of normal and imbedded bovine bone as measured by acoustic microscopy. Journal of Biomedical Materials Research 28, 931–938.